

Thermal and optical simulation of a photonic crystal light modulator based on the thermo-optic shift of the cut-off frequency

M. T. Tinker and J-B. Lee

Department of Electrical Engineering, University of Texas, Dallas, Texas 75083-0688
mtinker@utdallas.edu

Abstract: Ultra-compact device geometries requiring the development of new device technologies are essential for the successful implementation of active devices within photonic crystal systems. The basic operation of an ultra-compact silicon-based photonic crystal light modulator actuated by the thermo-optic modulation of the cut-off frequency about the telecommunication wavelength is discussed. A device design using highly localized high temperature resistive heating of heavily doped heating elements situated directly parallel to the photonic crystal light modulator was developed and evaluated using finite difference time domain and finite element analysis. These devices exhibited high extinction ratios and low insertion losses over a 40 nm frequency band around the telecommunication wavelength of 1550 nm with response times on the order of a few to several microseconds. The reliability implications of using these types of devices are discussed.

© 2005 Optical Society of America

OCIS codes: (130.3120) Integrated Optics Devices; (230.4110) Modulators; (230.7400) Waveguides, Slab

References and links

1. Y. A. Vlasov, N. Moll, and S. J. McNab, "Mode mixing in asymmetric double-trench photonic crystal waveguides," *J. Appl. Phys.* **95**, 4538-4544 (2004).
2. S. J. McNab, N. Moll, and Y. A. Vlasov, "Ultra-low loss photonic integrated circuit with membrane-type photonic crystal waveguides," *Opt. Express* **11**, 2927-2939 (2003), <http://www.opticsexpress.org/abstract.cfm?URI=OPEX-11-22-2927>.
3. M. Notomi, A. Shinya, K. Yamada, J. Takahashi, C. Takahashi, and I. Yokohama, "Structural tuning of guiding modes of line-defect waveguides of silicon-on-insulator photonic crystal slabs," *IEEE J. Quantum Electron.* **38**, 736-742 (2002).
4. S. Y. Lin, E. Chow, S. G. Johnson, and J. D. Joannopoulos, "Demonstration of highly efficient waveguiding in a photonic crystal slab at the 1.5- μm wavelength," *Opt. Lett.* **25**, 1297-1299 (2000).
5. M. Loncar, D. Nedeljkovic, T. Doll, J. Vuckovic, A. Scherer, and T. P. Pearsall, "Waveguiding in planar photonic crystals," *Appl. Phys. Lett.* **77**, 1937-1939 (2000).
6. T. F. Krauss, "Planar photonic crystal waveguide devices for integrated optics," *Phys. Status Solidi A*, **197**, 688-702 (2003).
7. Y. Sugimoto, N. Ikeda, N. Carlsson, K. Asakawa, N. Kawai, and K. Inoue, "Light-propagation characteristics of Y-branch defect waveguides in AlGaAs-based air-bridge-type two-dimensional photonic crystal slabs," *Opt. Lett.* **27**, 388-390 (2002).
8. S. Y. Lin, E. Chow, J. Bur, S. G. Johnson, and J. D. Joannopoulos, "Low-loss, wide-angle Y splitter at $\sim 1.6\text{-}\mu\text{m}$ wavelengths built with a two-dimensional photonic crystal," *Opt. Lett.* **27**, 1400-1402 (2002).
9. Y. A. Vlasov and S. J. McNab, "Losses in single-mode silicon-on-insulator strip waveguides and bends," *Opt. Express* **12**, 1622-1631 (2004), <http://www.opticsexpress.org/abstract.cfm?URI=OPEX-12-8-1622>.
10. Y. A. Vlasov and S. J. McNab, "Waveguiding in silicon-on-insulator photonic crystal and single-mode strip waveguides," in *2004 IEEE LEOS Annual Meeting Conference Proceedings* (Institute of Electrical and Electronics Engineers, New York, 2004), pp. 809-810 Vol 2.
11. R. M. De La Rue, "Photonic crystals and photonic wires for a nanophotonic future?," in *Proceedings of 2004 6th International Conference on Transparent Optical Networks* (Institute of Electrical and Electronics Engineers, New York, 2004), pp. 282-284, Vol 1.

12. W. Bogaerts, R. Baets, P. Dumon, V. Wiaux, S. Beckx, D. Taillaert, B. Luyssaert, J. Van Campenhout, P. Bienstman, and D. Van Thourhout, "Nanophotonic waveguides in silicon-on-insulator fabricated with CMOS technology," *J. Lightwave Technol.* **23**, 401-412 (2005).
13. E. P. Kosmidou, E. E. Kriezis, and T. D. Tsiiboukis, "Analysis of tunable photonic crystal devices comprising liquid crystal materials as defects," *IEEE J. Quantum Electron.* **41**, 657-665 (2005).
14. F. Du, Y.-Q. Lu, and S.-T. Wu, "Electrically tunable liquid-crystal photonic crystal fiber," *Appl. Phys. Lett.* **85**, 2181-2183 (2004).
15. C.-Y. Liu and L.-W. Chen, "Tunable photonic crystal waveguide coupler with nematic liquid crystals," *IEEE Photonics Technol. Lett.* **16**, 1849-1851 (2004).
16. M. W. Geis, S. J. Spector, R. C. Williamson, and T. M. Lyszczarz, "Submicrosecond submilliwatt silicon-on-insulator thermo-optic switch," *IEEE Photonics Technol. Lett.* **16**, 2514-2516 (2004).
17. E. A. Camargo, H. M. H. Chong, and R. M. De La Rue, "2D photonic crystal thermo-optic switch based on AlGaAs/GaAs epitaxial structure," *Opt. Express* **12**, 588-592 (2004), <http://www.opticsexpress.org/abstract.cfm?URI=OPEX-12-4-588>.
18. H. M. H. Chong, and R. M. De La Rue, "Tuning of photonic crystal waveguide microcavity by thermo-optic effect," *IEEE Photonics Technol. Lett.* **16**, 1528-1530 (2004).
19. Y. Sugimoto, N. Ikeda, N. Carlsson, K. Asakawa, N. Kawai, and K. Inoue, "Fabrication and characterization of different types of two-dimensional AlGaAs photonic crystal slabs," *J. Appl. Phys.* **91**, 922-929 (2002).
20. G. P. Agrawal, *Fiber-Optic Communication Systems* (John Wiley & Sons, New York, NY, 2002).
21. L. Eldada, "Advances in telecom and datacom optical components," *Opt. Eng.* **40**, 1165-1178, (2001).
22. M. Bourouha, M. Bataineh, and M. Guizani, "Advances in optical switching and networking: past, present, and future," in *Proceedings IEEE SoutheastCon 2002* (Institute of Electrical and Electronics Engineers, New York, 2002), pp. 405-413.
23. G. E. Jellison and H. H. Burke, "The temperature dependence of the refractive index of silicon at elevated temperatures at several laser wavelengths," *J. Appl. Phys.*, **60**, 841-843 (1986).
24. G. Cocorullo and I. Rendina, "Thermo-optical modulation at 1.5 μm in silicon etalon," *Electron. Lett.* **28**, 83-85 (1992).
25. F. G. Della Corte, M. E. Montefusco, L. Moretti, I. Rendina, and G. Cocorullo, "Temperature dependence analysis of the thermo-optic effect in silicon by single and double oscillator models," *J. Appl. Phys.* **88**, 7115-7119, (2000).
26. G. Cocorullo, F. G. Della Corte, and I. Rendina, "Temperature dependence of the thermo-optic coefficient in crystalline silicon between room temperature and 550 K at the wavelength of 1523 nm," *Appl. Phys. Lett.* **74**, 3338-3340, (1999).
27. G. Ghosh, "Temperature dispersion of refractive indices in crystalline and amorphous silicon," *Appl. Phys. Lett.* **66**, 3570-3572, (1995).
28. M. Bertolotti, V. Bogdanov, A. Ferrari, A. Jascow, N. Nazorova, A. Pikhin, and L. Schirone, "Temperature dependence of the refractive index in semiconductors," *J. Opt. Soc. Am. B* **7**, 918-922 (1990).
29. H. H. Li, "Refractive index of silicon and germanium and its wavelength and temperature derivatives," *J. Phys. Chem. Ref. Data* **9**, 561-658 (1980).
30. M. Iodice, F. G. Della Corte, I. Rendina, P. M. Sarro, and M. Bellucci, "Transient analysis of a high-speed thermo-optic modulator integrated in an all-silicon waveguide," *Opt. Eng. (Bellingham)* **42**, 169-175 (2003).
31. A. Cutolo, M. Iodice, P. Spirito, and L. Zeni, "Silicon electro-optic modulator based on a three terminal device integrated in a low-loss single-mode SOI waveguide," *J. Lightwave Technol.* **15**, 505-518 (1997).
32. C. Z. Zhao, G. Z. Li, E. K. Liu, Y. Gao, and X. D. Liu, "Silicon on insulator Mach-Zehnder waveguide interferometers operating at 1.3 μm ," *Appl. Phys. Lett.* **67**, 2448-2449 (1995).
33. G. V. Treyz, P. G. May, and J.-M. Halbout, "Silicon Mach-Zehnder waveguide interferometers based on the plasma dispersion effect," *Appl. Phys. Lett.* **59**, 771-773 (1991).
34. G. V. Treyz, "Silicon Mach-Zehnder waveguide interferometers operating at 1.3 μm ," *Electron. Lett.* **27**, 118-120 (1991).
35. U. Fischer, T. Zinke, B. Schuppert, and K. Petermann, "Singlemode optical switches based on SOI waveguides with large cross-section," *Electron. Lett.* **30**, 406-408 (1994).
36. M. T. Tinker and J.-B. Lee, "Thermo-optic photonic crystal light modulator," *Appl. Phys. Lett.* **86**, 221111-1-3 (2005).
37. M. Notomi, K. Yamada, A. Shinya, J. Takahashi, C. Takahashi, and I. Yokohama, "Extremely large group-velocity dispersion of line-defect waveguides in photonic crystal slabs," *Phys. Rev. Lett.* **87**, 253902-1-4 (2001).
38. Q.-A. Huang and N. K. S. Lee, "Analysis and design of polysilicon thermal flexure actuator," *J. Micromech. Microeng.* **9**, 64-70 (1999).
39. Q.-A. Huang and N. K. S. Lee, "Analytical modeling and optimization for a laterally-driven polysilicon thermal actuator," *Microsystem Technologies* **5**, 133-137 (1999).
40. L. Que, J.-S. Park, and Y. B. Gianchandani, "Bent-beam electrothermal actuators -- Part I: Single beam and cascaded devices," *J. Microelectromech. Syst.* **10**, 247-254 (2001).
41. F. P. Fehlner, "Formation of ultrathin oxide films on silicon," *J. Electrochem. Soc.* **119**, 1723-1727 (1972).
42. Y. Kamigaki and Y. Itoh, "Thermal oxidation of silicon in various oxygen partial pressures diluted by nitrogen," *J. Appl. Phys.* **48**, 2891-2896 (1977).

43. F. P. Fehlner, "Low temperature oxidation of metals and semiconductors," *J. Electrochem. Soc.* **131**, 1645-1652 (1984).
44. E. A. Taft, "Thin thermal oxide on silicon," *J. Electrochem. Soc.* **131**, 2460-2461 (1984).
45. H. Kahn, R. Ballarini, and A. H. Heuer, "Dynamic fatigue of silicon," *Curr. Opin. Solid State Mater. Sci.* **8**, 71-76 (2004).
46. T. Namazu and Y. Isono, "High-cycle fatigue test of nanoscale Si and SiO₂ wires based on AFM technique," in *Proceedings IEEE Sixteenth Annual International Conference on Micro Electro Mechanical Systems* (Institute of Electrical and Electronics Engineers, New York, 2003), pp. 662-665.
47. T. Namazu and Y. Isono, "High-cycle fatigue damage evaluation for micro-nanoscale single crystal silicon under bending and tensile stressing," in *17th IEEE International Conference on Micro Electro Mechanical Systems* (Institute of Electrical and Electronics Engineers, New York, 2004), pp. 149-152.
48. M. Madou, *Fundamentals of Microfabrication* (CRC Press, Boca Raton, Fla. 1997).
49. T.-R. Hsu, *MEMS & Microsystems: Design and Manufacture* (McGraw-Hill Higher Education, New York, 2002).
50. *Properties of Silicon* (INSPEC, Institution of Electrical Engineers, London and New York, 1988).
51. M. Asheghi, K. Kurabayashi, R. Kasnavi, and K. E. Goodson, "Thermal conduction in doped single-crystal silicon films," *J. Appl. Phys.* **91**, 5079-5088 (2002).
52. W. C. O'Mara, R. B. Herring, and L. P. Hunt, *Handbook of Semiconductor Silicon Technology* (Noyes Publications, Park Ridge, N. J., 1990).
53. G. T. A. Kovacs, *Micromachined Transducers Sourcebook* (WCB/McGraw-Hill, New York, 1998).
54. The Engineering Tool Box, "Air properties," (2005), http://www.engineeringtoolbox.com/air-properties-8_156.html.
55. J. A. Collins, *Failure of Materials in Mechanical Design: Analysis, Prediction, Prevention* (John Wiley & Sons, New York 1993).

1. Introduction

Photonic crystals and photonic wires offer the potential to generate exceedingly small microcircuits capable of handling and manipulating light at dimensions on the order of microns. Two-dimensional (2D) photonic crystal slabs are particularly promising compared to their three-dimensional (3D) photonic crystal counterparts since they can be readily generated by processing technology already in place in the semiconductor industry. Considerable effort has been expended towards developing and characterizing photonic crystal waveguides in these types of systems with a special emphasis on expanding the available bandwidth available for propagation, minimizing the propagation losses, reducing the losses at the junctions and the bends of the waveguides, and on minimizing coupling losses [1-8]. Photonic wires are even a simpler technology that offers the potential for even higher bandwidth operation and lower propagation losses and bending losses than seen in photonic crystal devices [9-12].

Despite the considerable effort being made to optimize the performance of passive devices, much less progress had been made towards actually implementing active devices within these types of systems [13-19]. This effort has been hampered in part by the fact that most active optical devices range in size from several hundred microns to a few millimeters as a result of the weak optical effects exhibited by most standard materials [20-22]. Although integrating active devices of this size within either photonic crystal waveguides or photonic wires might offer some technical advantages, the full potential of these systems cannot truly be realized until new technologies are developed that can achieve ultra-compact active devices in these types of systems. This is a major technological challenge that will require new and innovative concepts that will most likely be achieved by taking advantage of either the unique optical characteristics of these systems or by taking advantage of the small sizes of these systems to enable new device concepts previously unattainable in older technologies.

Although most of this research effort has been focused in the area of liquid crystal devices because of the large changes that can be induced in their refractive index, thermo-optic devices also offer several distinct advantages over other technologies that could aid in achieving ultra-small devices. Firstly, thermo-optic devices have the potential to achieve ultra-compact optical devices because of the relatively large changes that can be induced in the refractive index in these devices by the thermo-optic effect [23-29]. Secondly, thermo-optic devices can also generate thermal response times on the order of microseconds, or around 100 to 1000X faster than the millisecond response times generated by liquid crystal

devices. Finally, thermo-optic devices can also be readily integrated into the ultra-small geometries commonly used for either photonic crystal or photonic wire devices [13-18,20-22,30].

Modulators are one key component of many optical systems. The size of silicon-based modulators using traditional technologies typically varies from several hundred micrometers to millimeters in length [30-35]. Consequently, other types of solutions must be devised. A very compact thermo-optic photonic wire modulator of around 250 μm in total length has already been demonstrated using a Si-based Mach-Zehnder interferometer [16]. The extinction ratio was around -20 dB and the insertion loss as little as 2 to 3 dB. The insertion loss was primarily caused by the electrical contacts to the device. Measured response time was around 600 ns, excellent for a thermo-optic device. An even more compact thermo-optic modulator of around 20 μm in size has also been demonstrated in a photonic crystal waveguide by using a GaAs-based Mach-Zehnder interferometer by elevating the temperature to 250 $^{\circ}\text{C}$ [17]. However, the extinction ratio of the device was only -14 dB and the insertion loss very high, near 13 dB. Most of this insertion loss was probably caused from a combination of the splitting and bending losses that occur in the Y-junctions of the interferometer and from pattern irregularity in the device and input/output mismatch. Finally, a thermo-optic tunable filter was also demonstrated in a photonic crystal device [18]. The resonance wavelength was shifted by 5 nm in this device with a quality factor of approximately 500. Although this work did not explicitly focus on the implementation of a modulator in this particular instance, it nonetheless demonstrated the ability to effectively control the performance of a photonic crystal device through the thermo-optic effect.

An ultra-compact photonic crystal modulator of only a few microns in size based upon the thermo-optic modulation of the cut-off frequency in a silicon-based photonic crystal waveguide has also been recently proposed [36]. Localized heating can cause significant shifts in the cut-off frequency of these devices and modulate the light. Such devices exhibit low insertion losses with large extinction ratios. This paper presents a complete theoretical and engineering analysis of an actual thermo-optic device based upon thermo-optic modulation of the cut-off frequency of a photonic crystal waveguide that can achieve low insertion losses, high extinction ratios, a compact device layout, reasonable power dissipation, and response times on the order of microseconds. This analysis can easily be extended to other materials systems with appropriate modifications.

2. Basic theory of operation

Cut-off occurs very abruptly within photonic crystal waveguides. Very importantly, small changes in the cut-off frequency can cause dramatic changes in the transmitted intensity over very short distances [36]. Consequently, the light intensity in a waveguide can be strongly modulated around the cut-off frequency by changing the position of the cut-off frequency by the thermo-optic effect. In addition, only a few to several microns of length are required to strongly modulate the intensity of the light. This offers the opportunity to strongly modulate light around the cut-off frequency by heating a highly compact modulator of only a few to several microns in length to a high temperature.

The location of the cut-off frequency of a W1 channel photonic crystal waveguide oriented in the Γ -K direction in the triangular lattice of a thin silicon slab was modeled by using the twenty column wide photonic crystal test structure shown in Fig. 1. This waveguide was designed using a lattice spacing of 390 nm with a diameter of 215 nm and a diameter to lattice spacing of 0.55 and a thickness of 200 nm. These dimensions were identical to that of a detailed spectroscopic study of silicon waveguides oriented in the Γ -K direction reported in the literature which had demonstrated a cut-off range between 1500 nm and 1560 nm [37]. This offered the distinct advantage of being able to model a fully characterized photonic crystal waveguide with cut-off frequencies very close to the telecommunication wavelength of 1550 nm. Further, an extensive analysis of this waveguide performed in Ref. 37 also showed that this waveguide is single-mode.

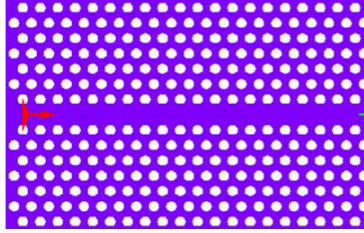


Fig. 1. Photonic crystal test structure showing Gaussian TE light source on left (red arrow) and detector on right (green cross).

The effective indices were calculated for this device by using analytical solutions to the transcendental waveguide equation for a 200 nm thick slab. A value of 3.50 was used for the refractive index of bulk silicon at 1550 nm. The refractive index of silicon was then varied about this value in order to account for the effect of material dispersion in silicon around this wavelength. The effective index was then calculated at various wavelengths. These values were then used to model the transmission spectrum of the waveguide by using a two-dimensional finite difference time domain (2D FDTD) analysis. Data from this analysis was then compared to the spectroscopic data from Ref. 37 in order to confirm the effectiveness of the modeling methodology.

The transmission spectrum of the system was determined by inputting a single frequency source of TE light into the waveguide in 10 nm increments in order to generate an accurate representation of the transmission characteristics of the system across a variety of wavelengths. The magnetic field amplitude of the system was measured by a detector placed at the output of the waveguide and the transmittance calculated by normalizing this output to the maximum magnetic field amplitude output from the waveguide. The transmittance calculated for this waveguide between 1200 nm and 1650 at 25 °C is shown in Fig. 2(a). The transmission spectrum exhibits a distinct cut-off range between 1500 nm and 1560 nm in almost exact agreement with the experimental data from the spectroscopic study [37].

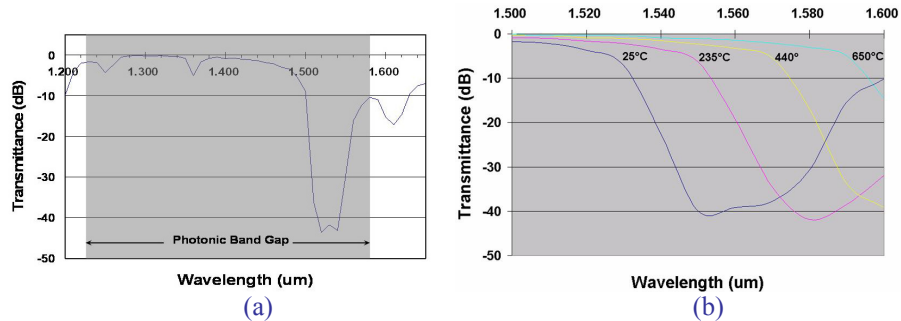


Fig. 2. (a) Modeled transmission spectrum across photonic crystal band gap at 25 °C and (b) shift of cut-off wavelength with temperature.

The position of the wavelength at the cut-off frequency was then slightly increased by increasing the lattice spacing of the photonic crystal lattice to 396 nm and the diameter to 218 nm while retaining the same diameter to lattice spacing in order to position the cut-off wavelength to just below 1550 nm. First the refractive index for this waveguide was calculated at 25 °C. The refractive indices were then calculated at elevated temperatures using the thermo-optic coefficient. Note that the thermo-optic coefficient is approximately $1.9 \times 10^{-4} \text{ } ^\circ\text{C}^{-1}$ at room temperature but rises steadily with increasing temperature. Consequently, the thermo-optic coefficient was estimated by using data acquired over a temperature range of several hundred degrees centigrade up to the expected operating temperature of the device. The value of the thermo-optic coefficient estimated from data acquired from a variety of different studies reported in the literature [23-29] averaged

approximately $2.4 \times 10^{-4} \text{ }^\circ\text{C}^{-1}$. This value was then used to calculate the refractive indices for silicon at 235 °C, 440 °C, and 650 °C. This resulted in an increase in the refractive index of approximately 0.05, 0.10, and 0.15 at these three temperatures and caused an increase in the cut-off wavelength of approximately 20 nm, 40 nm, and 60 nm as shown in Fig. 2(b). These spectra exhibit only a loss of a few dB before falling off abruptly at the cut-off wavelength to around -40 dB. Consequently, strong modulation can be achieved at the telecommunication wavelength of 1550 nm over a frequency band of between 20 to 60 nm by simply increasing the temperature.

An actual device was designed at the telecommunication wavelength of 1550 nm by using a modulator with a lattice spacing of 396 nm as shown in Fig. 3(a). The modulator was designed using a nine column wide waveguide having a width of $3.56 \text{ } \mu\text{m}$ to modulate the device. The modulator was subjected to a temperature of 425 °C, as shown in light blue, in order to simulate the effect of locally increasing the temperature of the device. Note that such highly localized heating was extremely effective at modulating the device. Since the remainder of the waveguide can be subjected to either 25 °C or 425 °C, the remainder of the device was designed using a lattice spacing of 415 nm so that the light could be transported into and away from the modulator at either temperature.

Note the strong ON/OFF characteristics of the device in Fig. 3(b) and Fig. 3(c). The modulator exhibited an extinction ratio of -30 dB in the OFF state and an insertion loss of only 1 dB in the ON state. Increasing the width of the modulator to eighteen columns increased the extinction ratio to -50 dB with little effect on the insertion loss. Note that placing the modulator within a photonic crystal waveguide appeared to significantly decrease the insertion loss of the device compared to the higher insertion losses determined from the test devices used to generate the data shown in Fig. 2.

Simulations were run to determine the effect of changing the width of the heat affected zone on the insertion loss. Decreasing the width of the heat affected zone to less than the width of the modulator starts to dramatically increase the insertion loss by causing the modulator to go into cut-off. However, increasing the width of the heat affected zone to a width greater than the width of the modulator has virtually no effect on the insertion loss. Consequently, actual devices can be designed using a heat affected zone that is only slightly greater than the width of the modulator thereby helping minimize the size of the device.

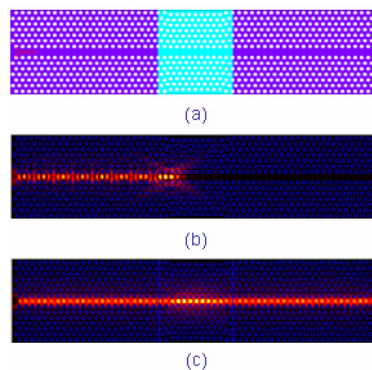


Fig 3. (a) Schematic diagram of thermo-optic modulator, (b) magnetic field amplitude of the modulator at 25 °C and 1550 nm, and (c) magnetic field amplitude at 425 °C.

3. Device design and analysis

A detailed engineering analysis was made to assess the feasibility of developing an actual thermo-optic device to modulate light in a photonic crystal waveguide by modulating the cut-off frequency of the device. ANSYS, a finite element modeling (FEM) software, was used to perform a steady-state and transient thermal analysis of this system to assess the temperature profile, power dissipation, transient response, and mechanical response of a

thermally activated photonic crystal device. Iterative designs were evaluated to optimize the device. A final design for this type of device is shown in Fig. 4 and discussed in detail below. This design can be altered in order to meet a wide varying set of device requirements.

3.1 Device design

Thermal actuation of this thermo-optic device is based upon the resistive heating of two highly doped parallel heating elements positioned directly adjacent to the modulator shown in the center of Fig. 4. The device is made from 200 nm thick silicon-on-insulator (SOI) silicon situated on top of 1.0 μm thick buried oxide (dark gray) bonded to $\langle 001 \rangle$ silicon. The device is 60 μm wide by 38 μm high and is doped to form two highly conductive regions of silicon (dark blue) directly adjacent to a highly resistive undoped silicon waveguide (light blue). The waveguide is patterned and etched to form the nine column wide modulator shown in Fig. 3 in order to modulate the device. Aluminum contacts are made directly to the doped silicon. Current is driven through the thermal heating elements positioned directly adjacent to the modulator by applying a voltage across the aluminum contacts. The waveguide is undercut with buffered oxide etch (BOE) in order to fully suspend both the photonic crystal waveguide and the heating elements.

The long narrow heating elements, nominally 1 μm high by 20 μm wide, were designed to generate a fairly uniform temperature distribution across the modulator. The variation in the temperature distribution in this area must be minimized to avoid any adverse effects on the high temperature modulation of the device. In addition, the close proximity of four thin 1.0 μm thick thermal oxide slabs grown directly on top of the silicon substrate directly adjacent to the modulator provides heat sinks which help to accelerate the speed of the device by accelerating the thermal transport of heat away from the heating elements. These heat sinks also work to limit the width of the temperature profile to the vicinity of the modulator. Also, the use of four fillets at the end of these heating elements not only helps accelerate the speed of the device by accelerating the thermal transport away from the thin heating elements but also helps to minimize the stress concentrators at these locations which could severely degrade the fatigue performance.

Undoped silicon is used in the waveguide to eliminate any optical absorption which would occur from doping the silicon. The doped silicon adjacent to the waveguide, however, is doped to around 10^{20} cm^{-3} in order to provide good electrical conduction in order to expedite resistive heating and to minimize the voltage drop across the device. Note that 1.5 μm of silicon is situated between the heating elements and the photonic crystal itself in order to accommodate the concentration gradient that would naturally form between the highly doped heating elements and the undoped photonic crystal waveguide.

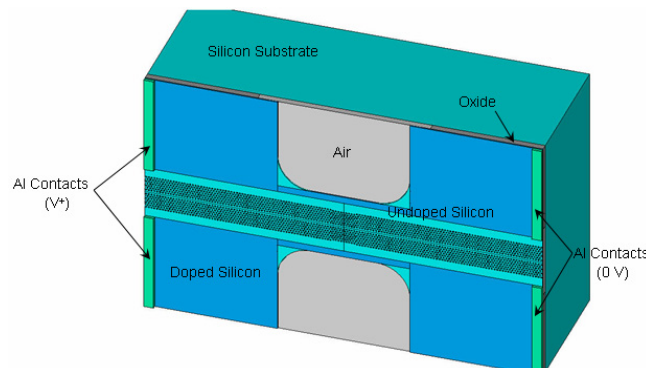


Fig. 4. Device design for thermo-optic device showing doped silicon (dark blue), undoped silicon (light blue), aluminum contacts (green), underlying oxide (dark gray) and air (light gray). Voltage applied across the device to drive current (device sectioned into four quadrants for ANSYS simulation).

3.2 Reliability constraints

Note that careful attention must be given to the reliability implications of using high temperature devices to modulate light. Oxidation is one of the most serious concerns. Note, however, that silicon MEMS actuators have routinely been heated to a temperature of around 650 °C for a number of years showing that the high temperature actuation of actual silicon devices is clearly feasible [38-40]. However, these actuators typically have thicknesses on the order of 2 μm or greater or around ten times greater than the 200 nm thickness required for this device. Consequently, this device must be operated at temperatures that are significantly less than 650 °C. Given the exponential decrease in the oxidation rate of silicon at these temperatures, this device could probably be successfully operated at temperatures as high as 550 °C. Estimates made from actual oxidation studies on silicon would generally agree with that estimate [41-44].

Fatigue is another major factor affecting the reliability of the device [45-47]. Unfortunately, fatigue in thin silicon films is strongly dependent on both the device size and the testing methodology and stress state applied to the silicon film. The maximum alternating stress that can be sustained by any particular geometry under any particular stress state can vary from a few hundred megapascals to a few gigapascals. In addition, surprisingly little fatigue data exists at elevated temperatures on thin silicon films making it difficult to assess the effect of temperature on fatigue. The available literature indicates that silicon fatigue exhibits virtually no dependence on temperature up to 300°C, the highest temperature for which data was available. In addition, silicon does not demonstrate any plastic deformation or creep beneath 800 °C [48]. Considering these data [46-48] in conjunction with the thermal actuator data [38-40] and the oxidation data [41-44] strongly suggests that this device should be capable of withstanding high cycle fatigue up to temperatures of around 550 °C.

Note that only sustained high temperature fatigue tests can clearly identify the maximum operating temperature of the device. Fortunately, modulating the device at lower temperatures, if necessary, would not destroy the functionality of the device but would simply reduce the available bandwidth for modulation. Consequently, light could still be successfully modulated by these types of devices at temperatures as low as 200 to 300 °C if operation at more elevated temperatures cannot be sustained.

3.3 Steady-state thermal analysis

ANSYS was used to model both the temperature profile and power dissipation generated during operation of the device by using a maximum allowable temperature of 500 °C. The temperature profile was modeled by balancing the heat flow being generated by the resistive heating elements against the heat flow being transported away from these elements. Because of the high thermal conductivity of silicon versus air, around 5,000 to 1 [38], most of the heat was transported away from the heating elements by the thermal conduction of heat through the SOI silicon. This heat was then transported down through the insulating oxide to the underlying silicon substrate. However, a significant fraction of heat was also transported through the underlying air down to the underlying silicon substrate. This was facilitated by the relatively large area available for thermal transport and because of the proximity of the highly conductive silicon substrate only 1 μm beneath the device. The fraction of heat transported away from the heating elements by the air above the device was relatively small because of the absence of a fast diffusing heat sink above the device and was ignored because of the large number of additional elements needed to simulate this effect.

The values of the various material properties used in this computation are shown in Table 1 [49-54]. The values used for silicon and for air are also given as a function of temperature since both are subjected to temperatures far above room temperature. The values used for the thermal conductivity and electrical resistivity of silicon are also given as a function of doping concentration since both vary strongly with doping.

Note that the thermal conductivity of the silicon decreases markedly with both temperature and with the doping concentration thereby reducing the lateral spread of the heat distribution

at elevated temperatures and within areas of highly doped silicon. The electrical resistivity of undoped silicon also decreases markedly at elevated temperatures as a consequence of the exponential increase in the intrinsic carrier density with temperature. Nonetheless, the resistivity is still around one hundred times higher than that of highly doped silicon between 400 to 500 °C and should not appreciably effect the operation of the device.

Table 1. Material Properties Used for ANSYS Simulation

Material	Properties	25 °C	100 °C	200 °C	300 °C	400 °C	500 °C	600 °C
Silicon	k (W/m°C) Doped	60	53	43	39	37	35	33
	k (W/m°C) Undoped	150	111	77	61	51	42	35
	C _p (J/kg°C)	713	766	819	844	861	878	895
	Density (kg/m ³)	2328	2327	2326	2323	2320	2317	2315
	Thermal Expansion (10 ⁻⁶ °C ⁻¹)	2.62	3.08	3.52	3.77	3.96	4.12	4.18
	C ₁₁ (GPa)	165.6	164.8	163.7	162.6	161.4	160.3	159.2
	C ₁₂ (GPa)	63.9	63.6	63.2	62.7	62.3	61.8	61.4
	C ₄₄ (GPa)	79.5	79.2	78.7	78.2	77.7	77.3	76.8
	Resistivity (Ω-m) Doped	1.0e-05						
	Resistivity (Ω-m) Undoped	2.3e+03	2.3e+01	4.7e-01	3.8e-02	6.3e-03	1.7e-03	6.2e-04
Air	k (W/m°C)	0.026	0.031	0.039	0.045	0.052	0.058	0.064
	C _p (J/kg°C)	1005	1009	1026	1047	1068	1089	1110
	Density (kg/m ³)	1.19	0.95	0.75	0.62	0.52	0.48	0.44
Oxide	k (W/m°C)	1.3						
	C _p (J/kg°C)	1000						
	Density (kg/m ³)	2270						
	Thermal Expansion (10 ⁻⁶ °C ⁻¹)	0.5						
	Young's Modulus (GPa)	70						
	Poisson's Ratio	0.20						
	Resistivity (Ω-m)	1.0e+14						
Aluminum	k (W/m°C)	236						
	C _p (J/kg°C)	942						
	Density (kg/m ³)	2700						
	Thermal Expansion (10 ⁻⁶ °C ⁻¹)	25						
	Young's Modulus (GPa)	70						
	Poisson's Ratio	0.35						
	Resistivity (Ω-m)	2.7e-08						

The lower half of the device shown in Fig. 4 was simulated using ANSYS by employing the symmetry of the system to reduce the size of the simulation. This allowed a significantly finer mesh size to be generated in order to simulate the device and also permitted the temperature profiles generated both normal and parallel to the surface to be viewed simultaneously. The device was meshed using the ANSYS SmartSizing mesh algorithm. These mesh matrices are shown in Fig. 5(a) and 5(b). The mesh algorithm generated an extremely fine mesh matrix in the extremely dense photonic crystal structure surrounding the air holes. The density of the mesh matrix decreased markedly in less dense areas of the device. Nonetheless, nearly 400,000 elements were required to model the device.

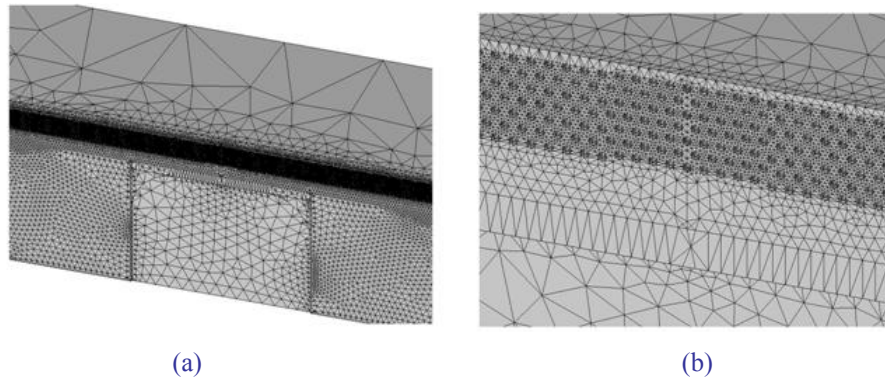


Fig. 5. (a) Lower magnification and (b) higher magnification of mesh matrices showing highly dense mesh matrix surrounding photonic crystal air holes.

The boundary conditions were set up to generate a maximum operating temperature of around 500 °C in the heating element. A positive voltage of 3.25 V was applied to the top of the aluminum contact on the left hand side of the device while the top of the aluminum contact on the right hand side was set to ground in order to generate the necessary current required to heat the device to 500 °C. The thickness of the simulated device was set to 20 μm thick in order to assure that the temperature on the backside of the device was at room temperature. The temperature on the backside of the device could then safely be set to 25 °C. The voltage was also set to ground on the backside of the device in order to simulate the effect of grounding the backside of the device.

The temperature profiles generated for this device are shown in Fig. 6(a) and 6(b) below. The maximum temperature of the device reached 496 °C in the center of the heating element and around 420 °C in the center of the modulator. Note that the temperature varies by only 30 to 40 °C within the modulator. This is around 10% of the total temperature variation of the device. This is a direct result of the long, narrow design of the heating elements used to heat the modulator. Also, the temperature distribution falls off to almost room temperature within around 25 μm of the center of the device as a direct result of placing the oxide heat sinks in close proximity to the modulator. Also note that almost the entire temperature drop underneath the modulator occurs across the air bridge as a consequence of the large thermal conductivity of the underlying silicon compared to the thermal conductivity of the air. The total power generated from the entire device is only 16.8 mW. This is a direct result of the extremely small size of the modulator and the adjacent areas of the device.

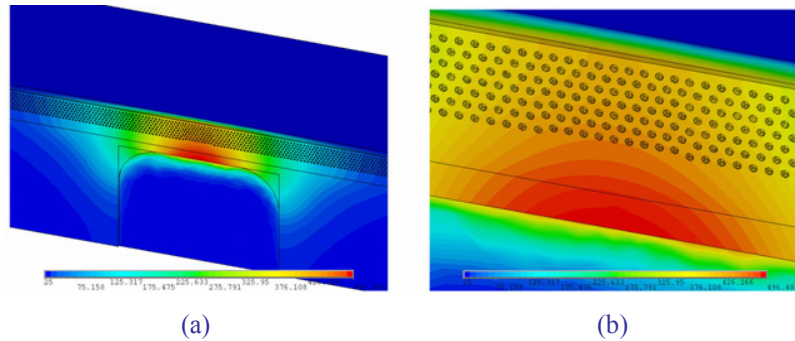


Fig. 6. (a) Lower magnification and (b) higher magnification of the temperature profiles showing the relatively uniform temperature distribution across the modulator, the rapid fall off in temperature across the device, and the shallow temperature profile beneath the device.

The refractive indices of the silicon were generated from the temperature profile shown in Fig. 6 at various temperatures. These refractive indices were overlaid with the waveguide shown in Fig. 7 in order to simulate the optical response of the waveguide by FDTD. The refractive indices were calculated by using the average temperature for each region used in the analysis.



Fig. 7. Refractive index profile generated from temperature profile shown directly above.

The magnetic field amplitude generated across the device at 25 °C and 1550 nm is shown in Fig. 8(a) and the magnetic field amplitude generated across the device by applying the temperature gradient shown in Fig. 6 to the device is shown in Fig. 8(b). Note the strong ON/OFF characteristics of the device. The modulator exhibits an extinction ratio of around

-33 dB at 25 °C and shows an insertion loss of only 1 dB at 420 °C. Note that the extinction ratio of the modulator can also be increased significantly by increasing the width of the device with little effect on the insertion loss.

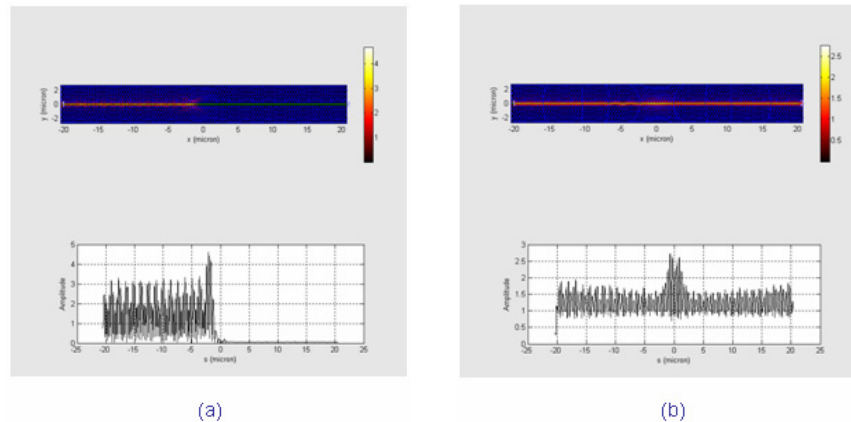


Fig. 8. (a) Magnetic field amplitude of thermo-optic modulator at 25 °C and (b) with the actual temperature gradient applied to heat the modulator to 420 °C at 1550 nm [Click on Fig. 8a (513 kB) and Fig. 8b (689 kB) to start movies].

The movies attached to Fig. 8(a) and Fig. 8(b) more clearly demonstrate the actual operation of the device. At 25 °C the light is transmitted down the waveguide until it reaches the modulator at which point it becomes strongly reflected back out of the waveguide. This creates a strongly pulsating beam as the incoming and reflected irradiation constructively and destructively interfere inside the waveguide. Raising the temperature to 420 °C causes the wavelength of the cut-off frequency to increase causing the light to be transmitted straight through the waveguide. The light slows as it passes through the modulator since the light is closer to the cut-off frequency in the modulator than in the remainder of the waveguide causing the intensity of light inside the modulator to increase relative to the waveguide [37].

The transmittance of this device is shown in Fig. 9 at both 25 °C and at 420 °C. Note the abrupt decrease in the intensity of light starting at 1530 nm at 25 °C and at 1570 nm at 420 °C. The extinction ratio is approximately -25 to -35 dB across this entire frequency range with very little insertion loss. The transmittance of the device begins to increase at 1570 nm to 1580 nm at 25 °C as the wavelength approaches the upper band gap of the modulator and the light begins to penetrate into the photonic crystal [36]. However, the waveguide adjacent to the modulator also begins to go into cut-off near these same wavelengths thereby cutting off the transmission of light through the entire device. Note that the 40 nm bandwidth over which this device can modulate the light would be insufficient to handle extremely high bandwidth applications but would be more than sufficient to handle less demanding applications such as modulating the channels within the 30 nm bandwidth of the conventional transmission band, or C-band, used within optical communication networks.

Three-dimensional FDTD was run at 1550 nm on this exact same device to confirm the effectiveness of using two-dimensional FDTD simulations for predicting the performance of the device. Since three-dimensional simulations run approximately 100X slower than their two-dimensional counterparts, the analysis was restricted to only five column widths on each side of the modulator. Also, the time needed to achieve a steady-state condition in the device was reduced as much as practicable along with the mesh size needed for simulation. A 0.5 μm thick air layer was used to simulate the device.

The three-dimensional magnetic field amplitude for both the OFF and ON states are shown in Fig. 10(a) through Fig. 10(d). The OFF state shown in Fig. 10(a) and Fig. 10(b) again exhibits an abrupt cut-off at 25 °C. The cross-sectional analysis in Fig. 10(b) shows that the light being reflected by the modulator at 25 °C continues to be totally restricted to the

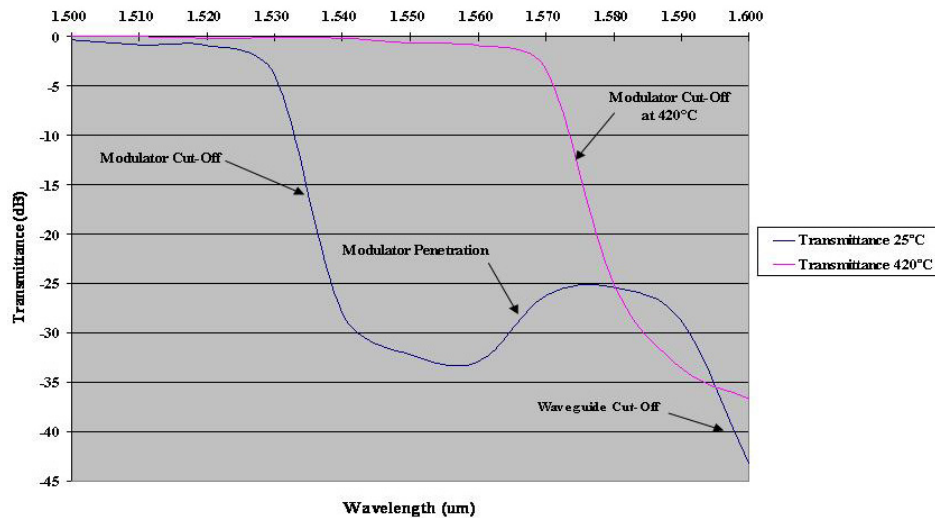


Fig. 9. Transmission spectra of modulated device.

waveguide. The modulator shows a high extinction ratio of around -34 dB very close to that generated by the two-dimensional simulation. The ON state shown in Fig. 10(c) and Fig. 10(d) again shows little insertion loss across the device. Again the light is totally restricted to the plane of the waveguide and no noticeable loss occurs out of the plane of the device. Consequently, the two-dimensional FDTD analysis used to model this system seems to model the three dimensional response of the system extremely well.

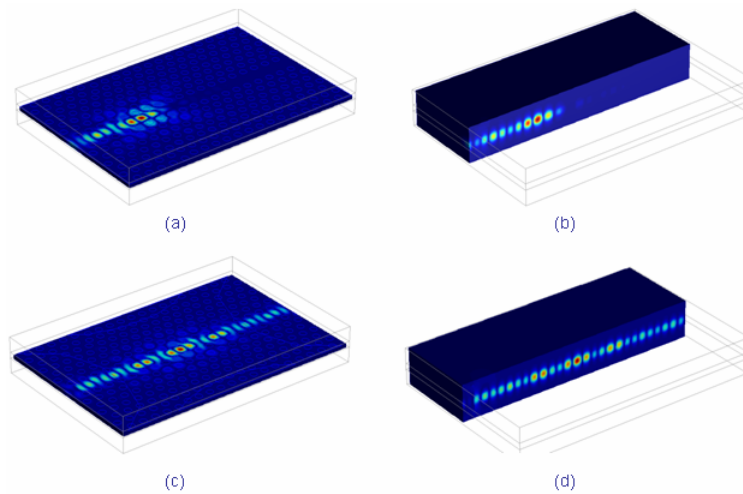


Fig. 10. (a) Oblique view of magnetic field amplitude of thermo-optic modulator generated by 3D FDTD at 1550 nm and 25 °C, (b) cross sectional view of modulator at 25 °C, (c) oblique view of modulator at 420 °C, and (d) cross sectional view of modulator at 420 °C.

3.4 Transient thermal analysis

A transient analysis was performed by using ANSYS to determine the rise and fall times required to thermally actuate the device. This analysis evaluated the transient response of the system every 0.2 μs over a total of 20 μs . Since this required an intensive amount of analysis requiring long processing times and large storage requirements, the actual structure shown in

Fig. 4 had to be simplified in order to facilitate the analysis. The structure used to model the transient response is shown in Fig. 11(a). The behavior of the photonic crystal device was modeled by using only silicon in the vicinity of the air holes by decreasing the thermal conductivity, the heat capacity, and the electrical conductivity in this region by the volume fraction of the air holes. This modification resulted in a 10X reduction in the number of elements needed to simulate the device. A steady-state thermal profile generated by applying 3.30 V across the device is shown in Fig. 11(b). The thermal profile is nearly identical to that obtained from the temperature profile of the actual device shown in Fig. 6 that was obtained by applying 3.25 V across the device confirming the effectiveness of using this simplified approach to model the system.

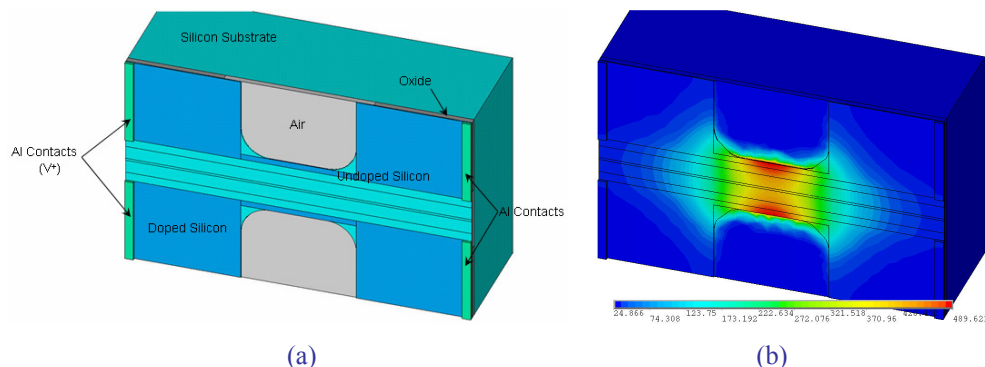


Fig. 11. (a) Transient analysis test structure and (b) steady-state thermal response of system [Click on Fig. 11(b) to start movie (1823 kB) and view transient response].

The movie attached to Fig. 11(b) clearly demonstrates the actual operation of the device. The device is heated through the long resistive heating elements in the center of the device and then spreads out sideways into the adjacent photonic crystal waveguide to give a fairly uniform temperature profile across the modulator. Once the device is turned OFF the heat dissipates quickly down the waveguide and out through the oxide heat sinks.

The ON and OFF characteristics are shown in Fig. 12(a) and Fig. 12(b), respectively. The device reaches a steady-state temperature of approximately 420 °C in the center of the device after 20 μ s. The rise time and fall times were then calculated between 10% and 90% of the final temperature. This particular device demonstrated a rise time of 5.6 μ s and a fall time of 3.5 μ s. The somewhat longer rise time can be attributed to the use of long, narrow heating elements that are only around 20% of the total width of the silicon bridge in the center of the device. The fairly rapid fall times can be attributed to the close proximity of the oxide heat sinks to the heating elements of the device. Typical ON/OFF characteristics are shown in Fig. 12(c) and 12(d). The 10 μ s ON/OFF characteristic shows a fairly stable and mature characteristic by 10 μ s while the 6 μ s ON/OFF characteristic is still rising slowly after 6 μ s. However, this characteristic has still risen to over 90% of the final steady-state temperature of the device by this time and would still prove useful for modulating the device. However, shorter times would probably not be feasible.

The performance could be improved by decreasing the rise time of the device by increasing the power generated by the resistive heating elements used to heat the device by employing the relation

$$P = I^2 R \quad (1)$$

where P is the power generated by the resistive heating elements, I is the current driven through the heating elements, and R is the resistance. For instance, increasing the width W of the heating elements would decrease R by $1/W$ while increasing I^2 by W^2 thereby increasing the rate of heating of the device and decreasing the rise time. However, thermal simulation of the device indicates that making this type of change may also degrade the uniformity of the

temperature profile and ultimately limit the width to which the heating elements can be increased. The device could also be initially ramped up to a higher voltage in order to quickly ramp up the temperature of the device before stepping down the device to the voltage required to sustain the device at its final steady-state temperature in order to increase the performance. With appropriate modifications the rise time of the device could potentially be reduced to much less than 1 μs . The performance of the device would then be limited by the fall time of the device which with this particular geometry is around 3.5 μs [16,30]

The fall time could also be decreased by changing the geometry of the device in order to increase the rate at which heat can be transported away from the heating elements to the oxide heat sinks. One obvious change would be to decrease the width of the silicon bridge in the center of the device in order to shorten the distance to the heat sinks. This would significantly increase the rate at which heat is transported away from the device and increase the performance. However, this same change would also decrease the width of the heat affected zone around the modulator and ultimately limit the width of the air bridge to around 10 μm . This would ultimately limit the maximum heat flux being transported away from the modulator to around two times that of a 20 μm bridge and limit the performance of the device to around 2 μs [30].

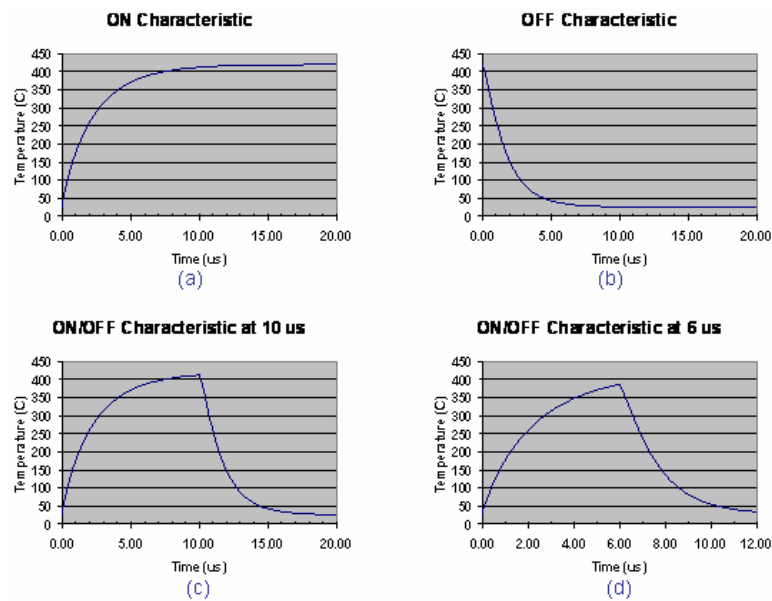


Fig. 12. (a) ON characteristic with rise time of 5.6 μs , (b) OFF characteristic with fall time of 3.5 μs , (c) 10 μs ON/OFF characteristic, and d) 6 μs ON/OFF characteristic.

3.5 Mechanical analysis

Since silicon is a brittle material the maximum normal stress theory was used in conjunction with the modified Goodman diagram to ascertain the failure criteria for high-cycle fatigue of the thermo-optic device shown in Fig. 4. Twelve different failure criteria can potentially cause failure using this type of analysis. However, only the most critical stress state will cause failure [55].

The residual stress state of the device was calculated in order to identify which stress state causes failure. The thermal stresses generated within the modulator were calculated using the structures shown in Fig. 5. The displacements were assumed to be zero around the outer edges of the device and in the vertical direction in the center of the device. The temperature profile shown in Fig. 6 was then overlaid over the element matrix shown in Fig. 5 in order to determine the thermal stresses generated within the modulator.

An analysis of the data revealed that the most critical stress state was the most negative principal stress state σ_3 . This stress state occurs as a direct result of the compressive residual stresses caused by the thermal expansion of the device. Note that the shape of the unit cell of the photonic crystal is distorted by less than 1 nm in any particular direction by this residual stress and should have no significant effect on the operation of the modulator.

A lower and higher magnification of the stress distribution of σ_3 is shown in Fig. 13(a) and Fig. 13(b). The most negative residual stress was generated at the bottom of a photonic crystal air hole in the center of the device. The residual stress generated at that location was -368 MPa. Consequently, the maximum alternating residual stress generated in the device at that point should equal -184 MPa. This stress level is probably insufficient to cause failure during long term operation of the device.

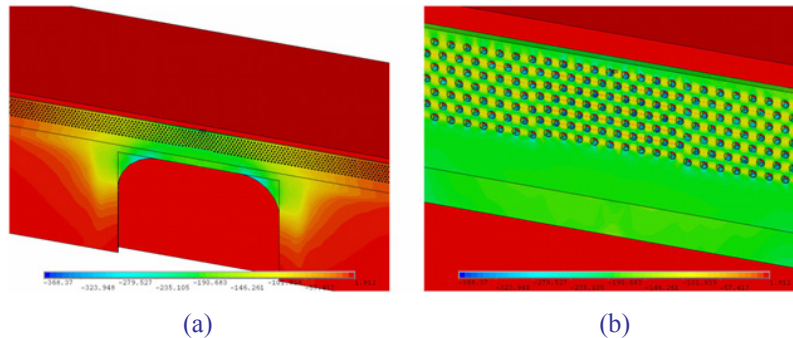


Fig. 13. (a) Lower magnification of σ_3 principal normal stress state and (b) higher magnification of σ_3 stress state showing maximum stress concentrated at bottom of photonic crystal air hole.

4. Conclusions

The basic operation of a photonic crystal device controlled by thermo-optic modulation of the cut-off frequency was discussed. Modulators with a high extinction ratio and low insertion loss are possible. An actual device was designed by using resistive heating of highly doped silicon heating elements positioned directly parallel to the photonic crystal light modulator in order to actuate the device. Devices actuated by temperature distributions generated across the light modulator exhibited high extinction ratios and low insertion loss. The temperature distribution extended only 25 μm from the center of the modulator and the resistive heating of the device generated only 16.8 mW of power. The rise time was 5.6 μs and the fall time 3.5 μs for this specific device. With appropriate design changes response times on the order of 2 μs could probably be achieved. A reliability analysis suggested that stress levels generated within this device would probably be insufficient to cause failure.